Submitted to *ASME Journal of Manufacturing Science and Engineering*

Effects of Build Angle on Additively Manufactured Aluminum Alloy Surface Roughness and Wettability

Christopher M. Bailey, Jordan A. Morrow, Emily M. Stallbaumer-Cyr, Cameron Weeks, Melanie M. Derby, Scott M. Thompson*

Alan Levin Department of Mechanical and Nuclear Engineering, Kansas State University, Manhattan, Kansas, U.S.A.

***Corresponding Author:** smthompson@ksu.edu, 785-532-5610

3002 Rathbone Hall, 1701B Platt St. Manhattan, KS 66506 USA

* Manuscript contains excerpts and figures from Conference Paper SHTC2021-63599 which was peer reviewed and presented at the ASME ES 2021 Summer Heat Transfer Conference

Abstract

Laser Powder Bed Fusion (LPBF) was utilized to create a series of aluminum alloy (i.e., AlSi10Mg) 5-mm-diameter support pillars with a fixed height of 5 mm containing varying filet angles and build orientations (i.e., 0˚, 10˚, 20˚, 30˚, 40˚, 50˚, and 60˚ from the normal surface) to determine their effects on surface roughness and water wettability. From experiments, anisotropic wetting was observed due in part to the surface heterogeneity created by the LPBF process. The powder-sourced AlSi10Mg alloy, typically hydrophobic, exhibited primarily hydrophilic behavior for build angles of 0˚ and 60˚, a mix of hydrophobic and hydrophilic behavior at build angles of 10˚ and 20˚, and hydrophobic behavior at 30˚, 40˚, and 50˚ build angles. Measured surface roughness, Ra, ranged from 5-36 μm and varied based on location. 3D-topography maps were generated and arithmetic mean heights, Sa, of 15.52-21.71 μm were observed; the anisotropy of roughness altered the wetting behavior, thereby prompting some hydrophilic behavior. Build angles of 30˚ and 40˚ provided for the smoothest surfaces. A significantly rougher surface was found for the 50º build angle. This abnormally high roughness is attributed to the melt pool contact angle having maximal capillarity with the surrounding powder bed. In this study, the critical melt pool contact angle was near-equal to the build angle suggesting a critical build angle exists which gives rise to pronounced melt pool wetting behavior and increased surface roughness due to enhanced wicking followed by solidification.

Keywords

Additive Manufacturing, Laser Powder Bed Fusion, Selective Laser Melting, AlSi10Mg, Heat Transfer, Vapor Chamber, Contact Angle.

Highlights

• Laser Powder Bed Fusion Additive Manufacturing was used to create pillars out of aluminum alloy AlSi10Mg.

• A critical build angle exists between 40º and 60º in which the melt pool has a contact angle ~50º which provides for maximal wetting behavior with the surrounding powder bed.

• The aluminum alloy powder is typically hydrophobic but showed mostly hydrophilic behavior at build angles of 0° and 60°.

• Build angles of 20° and 30° showed a mix of hydrophobic and hydrophilic behavior and 30°, 40°, and 50° showed hydrophobic behavior.

• Build orientation affected surface roughness, with 40° being the smoothest surface.

Introduction

The drive to create more powerful, yet increasingly small energy sources, has led to an issue of excessive heat flux in electronics packaging. High heat transfer within a concentrated area can result in electrical components overheating and/or warping. One solution to this problem is the use of a multi-phase heat spreader (i.e., thermal ground plane) such as a vapor chamber (VC) which effectively spreads heat within a hermetically-sealed hollow chamber (or cavity) using a working fluid and wicking structures [1, 2]. Vapor chambers utilize fluid phase change to create

temperature and pressure differentials, thereby promoting liquid and vapor slug movement throughout the cavity [3]. The design of a VC is somewhat limited in its geometrical complexity due to limitations in conventional manufacturing (e.g. end-milling, casting, etc.) and the need to integrate vacuum-grade joints to ensure hermetic sealing. In addition, wicking structures, which may exist as microchannels, sintered particles, or meshes, require cumbersome integration methods. With the use of layer-by-layer fabrication offered through additive manufacturing (AM) methods, such as Laser Powder Bed Fusion (LPBF), VCs with more complex geometric features are now possible [4,5].

Laser Powder Bed Fusion is an AM process commonly used for 'printing' metals. It uses a concentrated laser for selectively melting and fusing regions of a pre-deposited powder bed [6]. A thin layer of powder (e.g., 30 microns) is evenly spread across a build plate; subsequently, the laser melts select regions corresponding to a solid model path, and once the entire cross-sectional area of the part has been fused, another layer of powder is evenly applied on top of the previous layer. This process is repeated until the part has been completed [7].

There are several design parameters associated with LPBF. The orientation and location of the part during printing will influence the quality (e.g., roughness, porosity, geometry, mechanical properties) of the final part [8, 8a, 8b]. One such study observed that the printing orientation of LPBF AlSi10Mg deviated the R_a value of surfaces by as much as 5 μm, thus in some cases, creating stress concentrations leading to an over 50% reduction in fatigue strength [9]. Furthermore, unmelted powder within any channels and/or cavities within the part must be removed after LPBF.

The benefits of using AM to produce complex VC geometries include being able to design and manufacture optimized and/or conformal designs with as-printed wicking structures more

easily and cost effectively. In the study by Liu et al. [10] on the performance of VCs designed to mimic plant leaves, the process used to create the complex geometries ranged from chemical etching to graphite molding. The channel and wick designs employed were found to significantly improve heat transfer efficiency; however, the time and cost to produce such designs utilizing traditional manufacturing make scaled production of such VCs challenging. An experimental investigation was performed on a loop heat pipe with an additive-manufactured stainless steel primary wick cooling an 80-watt streetlamp. The heat transfer rate of the AM wick was 10% higher than a conventional wick loop heat pipe [11]. A porous regularly-patterned stainless steel wick structure created using selective laser melting technology was studied for its effective thermal conductivity, contact angle with multiple fluids (i.e., water, hexane, and ethylene glycol), and capillary performance. The wick showed improved capillary performance compared to sintered, mesh, or composite wicks; the large permeability was noted as the reason for the improved performance [12, 13]. A study conducted on the design of cooling layers for manufactured tooling determined that producing complex lattice structures via AM reduced cooling times within the cooling layers by 26% over a comparable design made utilizing traditional manufacturing methods [14]. Another study conducted on the feasibility of producing an oscillating heat pipe with Ti-6Al-4V found a 500% increase of thermal conductivity over a solid titanium alloy [15].

Within a heat pipe, it is important to understand the surface roughness and the wetting phenomena because of their direct effects on heat transfer. The effects of surface roughness in natural convection play a major role in heat transfer. Modifying the surface from a ‘smooth’ to a ‘rough’ surface with 9 mm pyramids improved the circulation within a fluid chamber such that it increased thermal transport by 76%. The change in surface roughness increased the number of “thermal plumes” which were responsible for enhanced heat transport [16].

The surface roughness also impacts the contact angle. The contact angle of a droplet affects the surface area of the liquid on a solid surface, which in turn effects the rate of heat transferred to the liquid. The rate of evaporation, and therefore heat transfer, has been found to change depending on how a liquid droplet interacts with a surface. Contact angles directly affect the thin film thickness of the liquid which is where the majority of evaporation heat transfer occurs [17]. For water, contact angles which are less than 90˚ (i.e., hydrophilic) generally have linear evaporation rates, whereas contact angles which are greater than 90˚ (i.e., hydrophobic) typically have non-linear evaporation rates [18]. The contact angle of water on AM AlSi10Mg is considered to be hydrophobic [19]. Contact angles in the context of VCs are most affected by heat transfer rate, solid heat transfer properties, liquid/gas heat transfer and fluid dynamics properties, surface roughness, internal surface geometries, and surface treatment. A droplet sitting on a surface will be in one of two states – Cassie or Wenzel. In the Cassie state, the droplet sits on top of the microscale ridges of the surface typically on pockets of air; in the Wenzel state, the droplet sits inside the microscale ridges of the surface and is pinned to the surface. Typically, when a surface is hydrophobic, increasing surface roughness will make the droplet more hydrophobic, and when a surface is hydrophilic, increasing surface roughness will make the droplet more hydrophilic. Both hydrophobicity and hydrophilicity have their advantages for heat transfer. In condensation, a hydrophobic surface sheds droplets faster to keep the liquid film resistance lower, thereby increasing heat transfer [20, 21]. In boiling, a hydrophilic surface is advantages to maintain a layer of liquid water on the heated surface, thereby minimizing the effect of dryout [22].

In general, the LPBF process can result in highly variable surface roughness [22a] and porosity due to the nature of the melting and solidification process [23]. Processes can be taken to change the surface conditions with coatings [24], remelting [25, 26] and adding microstructures

[27, 28] which can affect fluid contact angles. Parts made via LPBF are prone to having a surface roughness that varies along their perimeter – based on how that perimeter is oriented with respect to the build direction [29]. Surface portions that are facing upward are 'upskins' while surface portions facing downward, toward the substrate, are 'downskins' [30]. Upskin surfaces are typically smoother, due to there being more solidified material underneath them and gravity pushing the melt pool to spread along the surface more, while downskin surfaces are typically rougher as they interact more with the powder bed where capillary forces pull on the melt pool during processing.

Several studies have focused on understanding the process-structure-property relationships inherent to the LPBF of AlSi10Mg; in particular, how process factors such as laser power, laser beam diameter, layer thickness, and build orientation affect AM surface quality [31-36]. Although one can optimize the specific energy of the laser during LPBF to reduce surface roughness [31, 32], one can control surface roughness via part orientation. Even if one does not aim to control final part roughness, it is beneficial to understand how different oriented surfaces vary in terms of surface roughness, especially for those intending to use LPBF parts for thermal/fluid applications. Using a laser scanning microscope, Leis et al. [31] measured an effective surface roughness of 22.3 μm for the surface of each AlSi10Mg powder layer in their LPBF system. It is mentioned that the rough powder layer provides for variation in local absorptivity and thus uneven laser-to-part energy transmission. Li et al. [32] found that the surface roughness along the top face of their LPBF AlSi10Mg specimens was far less that that measured along the sides. However, Yu et al. [33] provide results demonstrating that the sides of their AlSi10Mg LPBF cubes were smoother than their top surface. This may be attributed to Yu et al. preheating the substrate to 200°C on their SLM Solution system; yet, this also demonstrates how the variability in LPBF system can lead to

unique surface roughness observations. Dong et al [34]. demonstrated that the net shape is closer for AlSo10Mg LPBF specimens (flat tensile bars) built at an angle relative to vertical specimens. Hofele et al. [35] investigated the effect of build angle on surface roughness of LPBF AlSi10Mg specimens and found that surface roughness generally decreases when going from a 0° (horizontal orientation) to a 60° build orientation. For the 45° oriented specimens, the downskin surface roughness was found to be nearly double that of the upskin. Arithmetic roughness (per ISO 4287) ranged between 8 and 19 μm. A maximum height variation of 170 μm was observed for the 0° sample due to the staircase effect. Gouveia et al. [36] printed various test artifacts from AlSi10Mg powder via LPBF. They found that the typical average roughness was around 8-12 μm and that regions with no support structure could possess up to 20% higher surface roughness. They also found higher variability in surface roughness measurements for top surfaces due to intermittent defects relative to side surfaces. The roughness of the top surface was found to be slightly higher than that of the sides with this difference becoming essentially zero when using the manufacturer-provided, default process parameters. This study aims to determine the effects of printing orientation surface roughness and fluid contact angles for as-printed LPBF AlSi10Mg surfaces. The relationship between the LPBF AlSi10Mg surface and surface wetting has not received significant attention in the literature. This study observed uncoated, untreated surfaces which would naturally be present inside of a heat pipe with no surface post processing, since in most heat pipe applications, the inclusion of surface coatings and treatments would involve expensive post processing which would require time-consuming and results of varying benefits. The study of different surface coatings and treatments in AM AlSi10Mg heat transfer applications may be beneficial for future studies. The information in this study will aid in the design considerations of printing orientation on multi-phase thermal heat spreaders. This study also seeks to provide

insights on surface roughness and fluid wetting behavior that will be present in such multi-phase thermal heat spreaders.

Specimen Design and Manufacturing

Specimens were fabricated via LPBF using spherical AlSi10Mg (cast aluminum alloy) powder (i.e., 10-45 μm normally-distributed diameters) as the raw material. This specific alloy was chosen due to its additive manufacturability, low cost, and relatively high thermal conductivity [37]. Although copper is the typical material-of-choice for thermal management media, it is a considerably more expensive material to manufacture via LPBF. It is also a much denser material making it less viable in applications requiring low weight thermal solutions. Currently, the processing of copper alloys via LPBF is still in development and not widespread. Hence, the use of LPBF of aluminum thermal management devices is of interest and the focus of this current study. The LPBF of all specimens were fabricated using LPBF services provided by Protolabs. Each layer was set to a thickness of 30 μm, providing for high resolution with tolerances of ± 0.1 mm. The specimens were manufactured with a GE Concept Laser M2 using a 370 W Nd:YaG fiber laser with a spot size of 200 μm and a scan speed of 1800 mm/s. The material composition provided was as follows: Al (87.1-89.35 weight %), Si (9-11%), Fe (0.55%), Cu (0.05%), Mn (0.45%), Mg (0.2-0.45), Ni (0.05), Zn (0.1), Pb (0.05%), Sn (0.5%), Ti (0.15%).

Seven specimens with dimensions shown in Fig. 1 were printed, each with its own build orientation/angle, ϕ (i.e.: 0˚, 10˚, 20˚, 30˚, 40˚, 50˚, and 60˚) normal to the build plate surface. All specimens had the same design consisting of 5-mm tall pillars with 5-mm diameters for potential use inside a VC. Such pillars provide chamber support and provide another means for mass and heat transfer via wicking [38]. Five pillar geometries with chamfer angles of 30˚, 25˚, 20˚, 15˚, and 10˚, were created to determine if there were significant effects on surface roughness with a

change in printing angle. The specimens were printed with the flat surface opposite the pillars as the base; meaning, the pillared surface was the 'upskin' of the part during LPBF. Apart from the pillar geometries, there was space on the upskin of the specimen which was intention6ally left flat to measure the surface roughness and contact angles which may represent VC surfaces within the cavity. As shown in Fig. 1, when changing the build angle, the orientation angle of the pillars changed. This effect on the upskin and downskin (identified in Fig. 1) surface roughness was investigated through microscopy of the pillar profiles.

Prior to any measurements, the specimens were rinsed with isopropyl alcohol, acetone, then water and then allowed dry. This cleaning process represents one used to clean and remove excess, entrapped metal powder from within a cavity of a VC manufactured via LPBF. Specimen surfaces were not coated in order to better represent the surfaces of as-printed, internal geometries. The typical procedure for the removal of excess metal powder within an internal geometry is to implement sealable ports into the side of the specimen, which enables it to be rinsed [15].

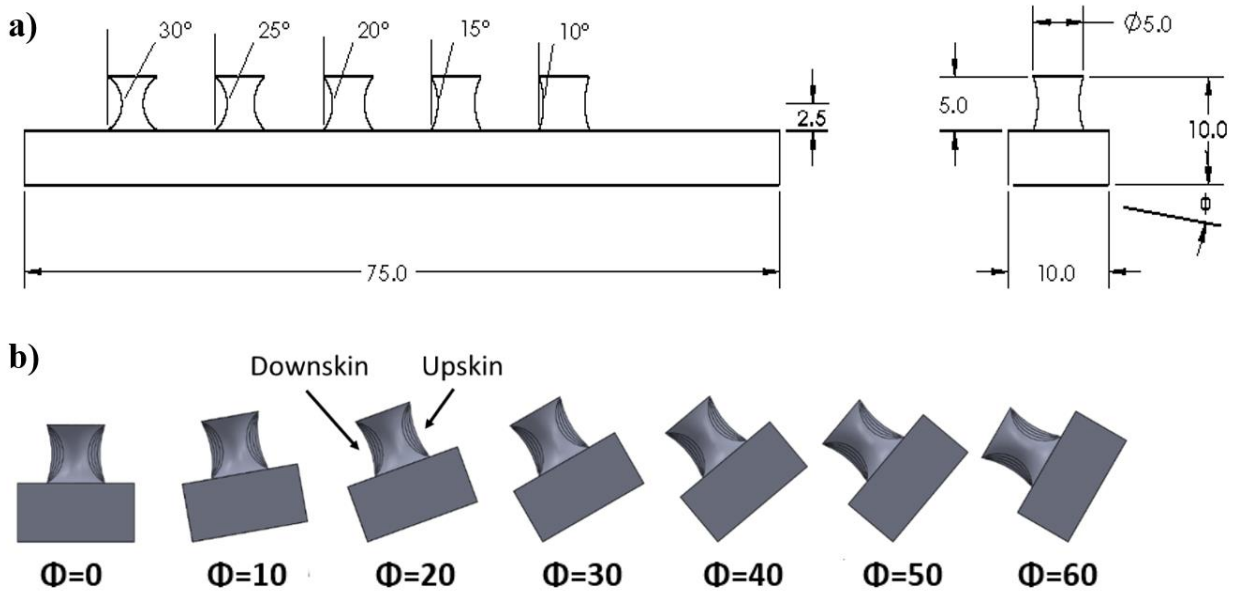

Figure 1. a) Specimen design including pillars with various chamfer angles; b) investigated orientation/build angles, ϕ, and upskin and downskin surface definitions. All dimensions are in millimeters.

Experimental Methods

To characterize the relationship of surface roughness and contact angles with build orientation of the AlSi10Mg specimens, two experiments were conducted. The first experiment aimed to determine the solid-liquid, initial contact angle, θ, with a 0.2 μL (± 0.08 μL) deionized water droplet on the flat portion of the upside of each specimen. The contact angle of the water droplet was measured using a digital goniometer (Allied Prosilica GC model # GC750 using the software FTA 32), the contact angles were measured using Photon FastCam Viewer 4, and the results were exported to a Microsoft Excel® spreadsheet for analysis (Fig. 2). The droplet was placed by hand on the specimen surface with the Fisher Brand Elite Adjustable-Volume pipette oriented as vertical as the goniometer allowed; the surface temperature was monitored using a type-T thermocouple (±1 $^{\circ}$C resolution) resting on the same sample surface as the droplet. Contact angle measurements were done at room temperature, nominally 22 ± 1 $^{\circ}$C.

Once the 0.2-μL water droplet had ceased moving from being placed on the specimen's surface, achieving a steady-state morphology, a picture (640x480 96 dpi) was taken which enabled the solid-liquid contact angle to be calculated by the digital goniometer software. The droplets would remain in a steady-state morphology for several minutes on the surface of the specimen at room temperature before completely evaporating. The contact angles of three water droplets placed in different locations on the flat surface of each specimen were measured by the digital goniometer, for a total of 42 contact angle measurements. The contact angles of both the left and right side of the two-dimensional water droplet image were obtained, and an average contact angle calculated from both the left and right contact angles was obtained from each droplet. The average contact angle of all three water droplets on each specimen was also calculated. An example image of a droplet with contact angle measurements obtained via the goniometer can be seen in Fig. 3. Note that the small weight of the droplets prevented any gravity influence on droplet morphology as shown by its Bond number, Bo, being much less than unity (details later discussed).

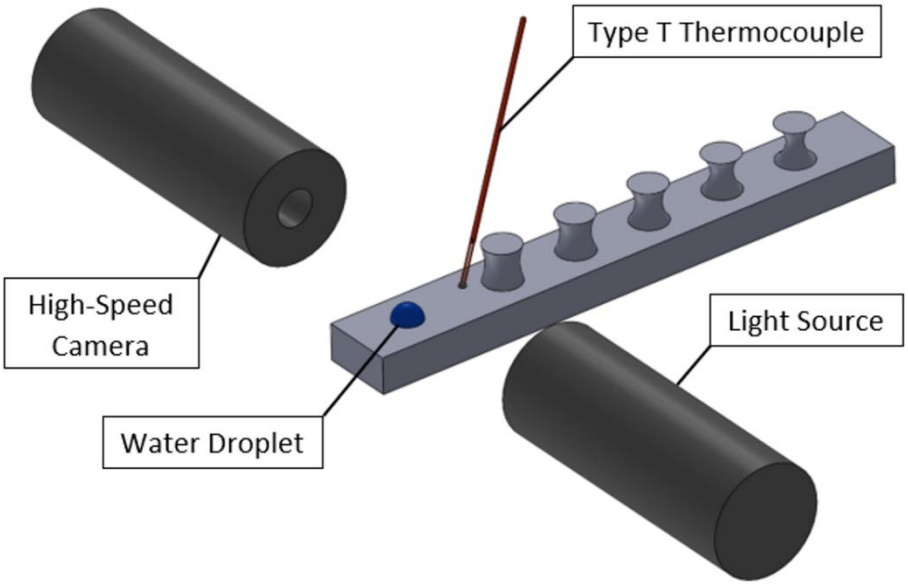

Figure 2. Schematic of contact angle measurement apparatus showing digital goniometer AM sample surface.

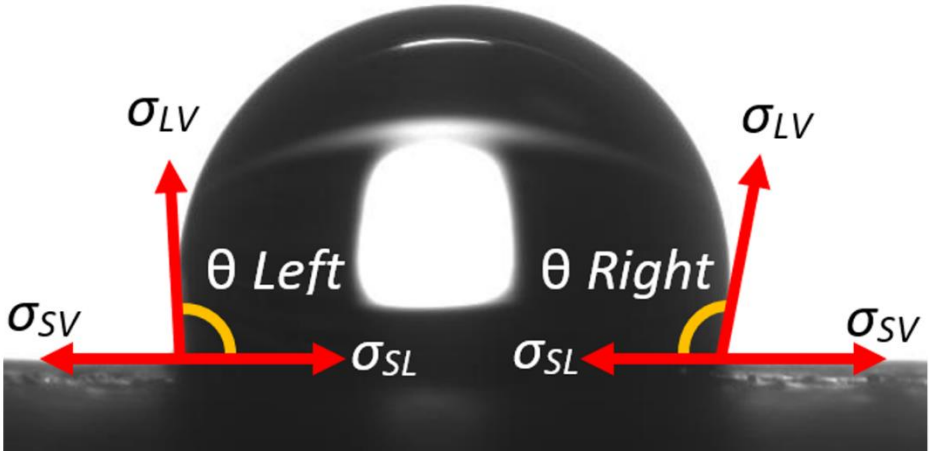

Figure 3. Example goniometer image of droplet on AM surface with solid-liquid contact angles labeled.

The second set of experiments focused on determining the impacts that build orientation and pillar geometry had on surface roughness. Several images of each specimen were taken utilizing an optical microscope (Amscope ME520T) magnified 5x. Side and top view images were taken of each flat surface and while only side view images (at two different magnifications) were taken for each pillar. The sides of each pillar were observed with the optical microscope to determine upskin/downskin variation and whether a significant and observable difference in surface roughness was present between chamfer angles on the same specimens. The pillar roughness profiles are important since, once incorporated into the internal geometry of a multi-phase heat spreader, they act as wicking structures. Because a majority of evaporation takes place in the bridging area near the solid-liquid interface, the surface of these structures implies the wetting behavior of liquid droplets; and therefore, heat transfer. The flat surfaces were important to observe to determine whether a trend between printing orientation and surface roughness, and consequentially, liquid contact angles was present. Figure 4 shows the pillar geometry and location of the pictures taken with an optical microscope for the specimens throughout this study.

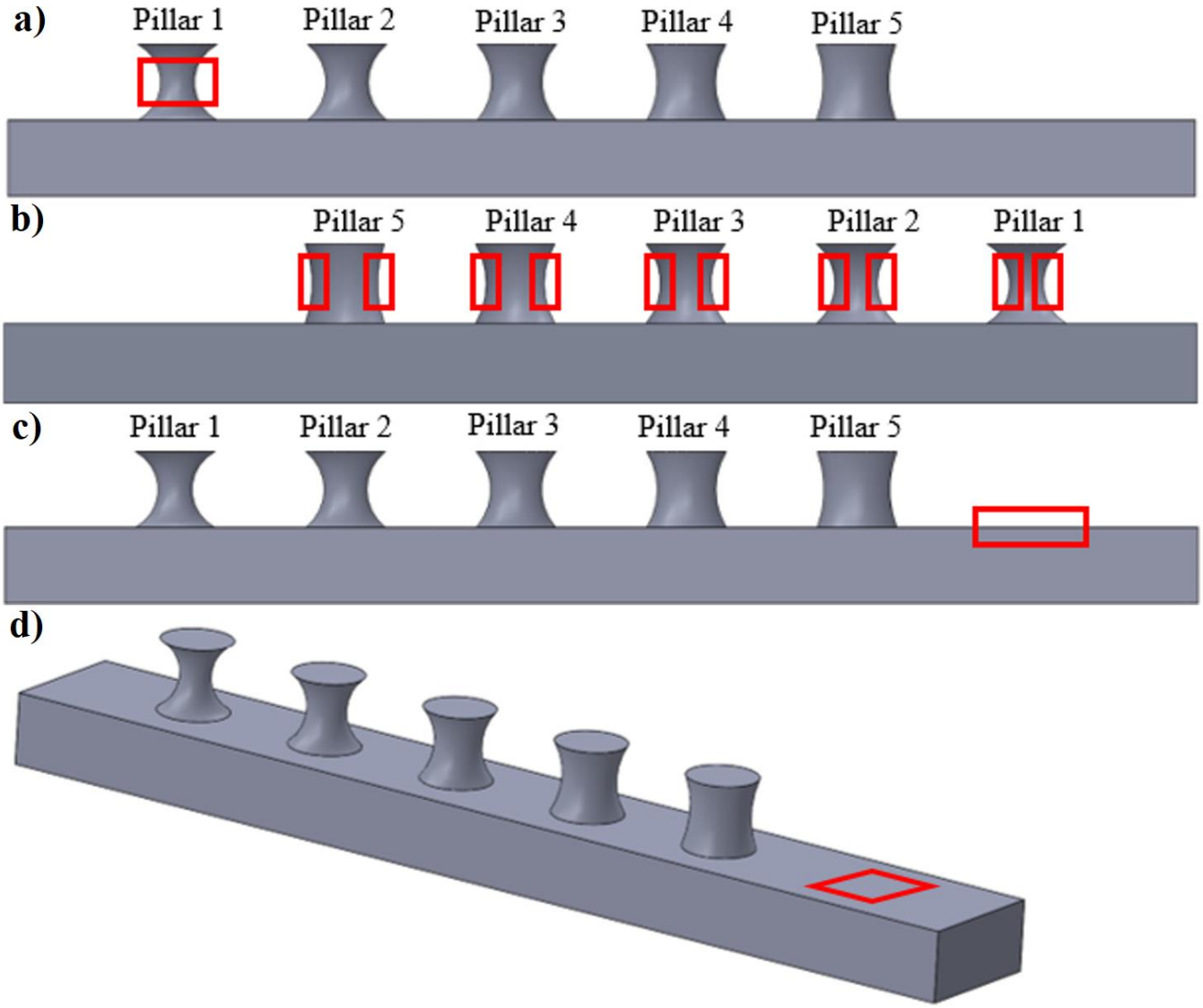

Figure 4. Pillar geometry and locations of images in Figs. a. (6) b. (7) c. (8) d. (9) & (14).

Once images had been taken using the optical microscope, the specimens were cut into 6 pieces so that they could be observed under a scanning electron microscope (SEM). SEM microscopy was performed using a Low Vacuum SEM (Model: Carl Zeiss EVO MA 10) operating at 5 kV. Due to the specifications of the microscope, the specimens could not fit into the observation platform without first being separated. Each of the pillars, as well as the flat portion of the specimens, were separated from each other and rinsed to remove contaminants.

Specimens were then measured for surface roughness at 5 locations via an EDM MVi5 profilometer with FANUC 5-Axis software. A roughness measurement was taken along the flat surface of each part in the same location that contact angles were previously recorded. Two different roughness measurements were taken on both the left (downskin) and right (upskin) sides of each 10˚ chamfer pillar. Theoretically, on the 0˚-built specimen, the downskin and upskin surface roughness values would be equivalent because their build orientation would be the same. One measurement was taken in a location with a large partially melted metal bead to obtain a value of high surface roughness and one measurement was taken in close proximity to this location such that there were relatively few partially melted metal beads. This was done on both the upskin and downskin sides of the pillars to obtain high and low surface roughness values to provide a more accurate surface characterization.

Results and Discussion

Contact angle measurements

A total of 42 initial contact angle measurements were recorded for the flat surface of each specimen and the results are shown in Table 1. To determine whether the values obtained in this study were statistically relevant, the parameter p-value was calculated using a single factor analysis of variance (ANOVA). The p-value was determined to be 0.001 which is less than the value 0.05 required to verify that the contact angle values obtained in this study were statistically relevant. AlSi10Mg alloy is typically hydrophobic [19]. However, data presented in Table 1 and Fig. 5 indicate that the build angle, ϕ, influences wettability and subsequent contact angle, θ. Variation was observed between the left-hand-side and right-hand-side contact angles (i.e., anisotropic wetting) for some droplets, indicating some nonuniformities in surface roughness and composition due to the LPBF manufacturing process. For build angles of 0˚ and 60˚, contact angles indicate

that the surface is primarily acting hydrophilicly, although the variance is larger for the 0˚ build angle. At build angles of 10˚ and 20˚, some droplets were hydrophilic on one side and hydrophobic on the other; it is possible that partially melted metal beads, as discussed in the following section, may contribute to this nonuniformity. For 30˚, 40˚, and 50˚ build angles, droplets consistently exhibited hydrophobic behavior and partially melted beads were smaller in diameter. It was observed that there was a higher amount of partially melted metal beads on the surface of the $\phi = 0^{\circ}$ specimen; upon contact with partially melted metal beads left over from the LPBF process, the water droplet would 'attach' itself via surface tension which greatly affected the contact angles [4,39,40]. As the printing angle increased, the surface became more water repellant until the experiments reached the fifth specimen (ϕ=40˚). It was observed that anisotropic wetting (i.e., left-hand-side and right-hand-side variation) generally decreased as the build angle increased. These trends indicate that the surface roughness decreases as the build angle increases, which allows for more droplet stability.

Table 1. Experimental contact angle measurements for 7 build orientations showing right and left contact angles.

Build Angle	Contact Angle [°]			
	Left	Right	Avg	Tot Avg
Φ=0°	43.7	67.3	55.5	74.4
	77.9	82.0	79.9	
	81.7	93.6	87.7	
Φ=10°	108.4	86.0	97.2	96.2
	107.5	96.1	101.8	
	83.3	95.9	89.6	
Φ=20°	90.4	82.9	86.6	88.3
	89.2	89.2	89.2	
	83.5	94.8	89.2	
Φ=30°	98.4	101.5	99.9	100.8
	106.1	98.0	102.0	
	100.8	100.3	100.5	
Φ=40°	109.7	114.5	112.1	106.7
	107.9	110.7	109.3	
	96.8	100.6	98.7	
Φ=50°	102.3	103.0	102.7	100.6
	100.2	98.6	99.4	
	99.3	100.3	99.8	
Φ=60°	84.5	83.2	83.9	82.8
	81.5	82.0	81.7	
	83.4	81.9	82.7	

A pure liquid in contact with its own vapor atop a smooth solid while under steady-state conditions has a contact angle which is a function of its interfacial surface tension. An equation relating surface tension and contact angle is Young's equation which states:

$$\sigma_{LV}\cos(\theta) = \sigma_{SV} - \sigma_{SL} \quad (1)$$

where σ is fluid surface tension, θ is the solid-liquid contact angle, and subscripts S, L, and V stand for solid, liquid, and vapor, respectively. For static fluid wetting of rough horizontal surfaces, Young's equation may be multiplied by roughness, γ, which is the ratio of the actual solid surface area, A_s, per unit of area projected on a horizontal plane, A_{hor}:

$$\gamma = \frac{A_s}{A_{hor}} \tag{2}$$

$$\cos(\theta) = \frac{(\sigma_{SV} - \sigma_{SL})}{\sigma_{LV}} \gamma \tag{3}$$

Per Young's equation, it is clear that roughness directly impacts contact angle. For a unity roughness, i.e. γ = 1, the contact angle is equivalent to that experienced on a smooth surface. For hydrophilic surfaces, roughness often decreases contact angle, whereas for hydrophobic surfaces, roughness can increase contact angle [41]. However, roughness alone is not sufficient to characterize a surface; these results demonstrate impacts of partially melted metal beads, which are nonuniform on the surface.

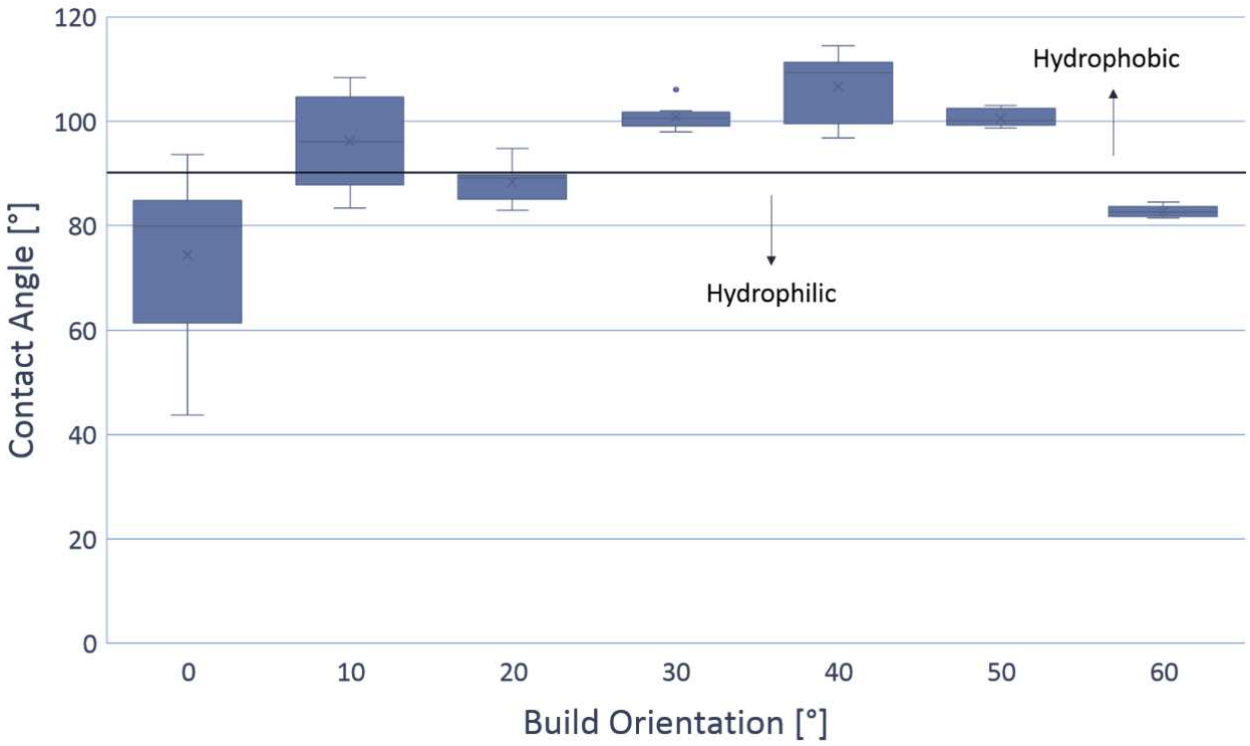

Figure 5. Distribution of contact angle measurements (whiskers denoting high, low and average values) for each investigated printing/orientation angle. The red (solid) line indicates 90°; the critical contact angle that separates hydrophobic (top side) and hydrophilic (bottom side) conditions.

Microscopy

Via optical microscopy, it was observed that the sides of the pillars along all seven specimens contained a considerable amount of partially melted beads. Per Ref. [23], the ratio between laser power and laser beam diameter, P_L/d_b, used in the LPBF of AlSi10Mg parts was optimum in the range of 3000 W/mm < P_L/d_b < 3500 W/mm. Values lower than 2000 W/mm generally led to the creation of partially melted metal beads and uneven roughness values [23]. For this study, P_L/d_b = 1850 W/mm, and this explains the excessive formation of partially melted metal beads on the specimens in this experiment. However, in the context of VCs, a large surface

area and a rough texture may in fact benefit heat transfer and bubble formation during fluid phase change [42]. Images of the partially melted metal beads on the pillars are shown in Figs. 6–7.

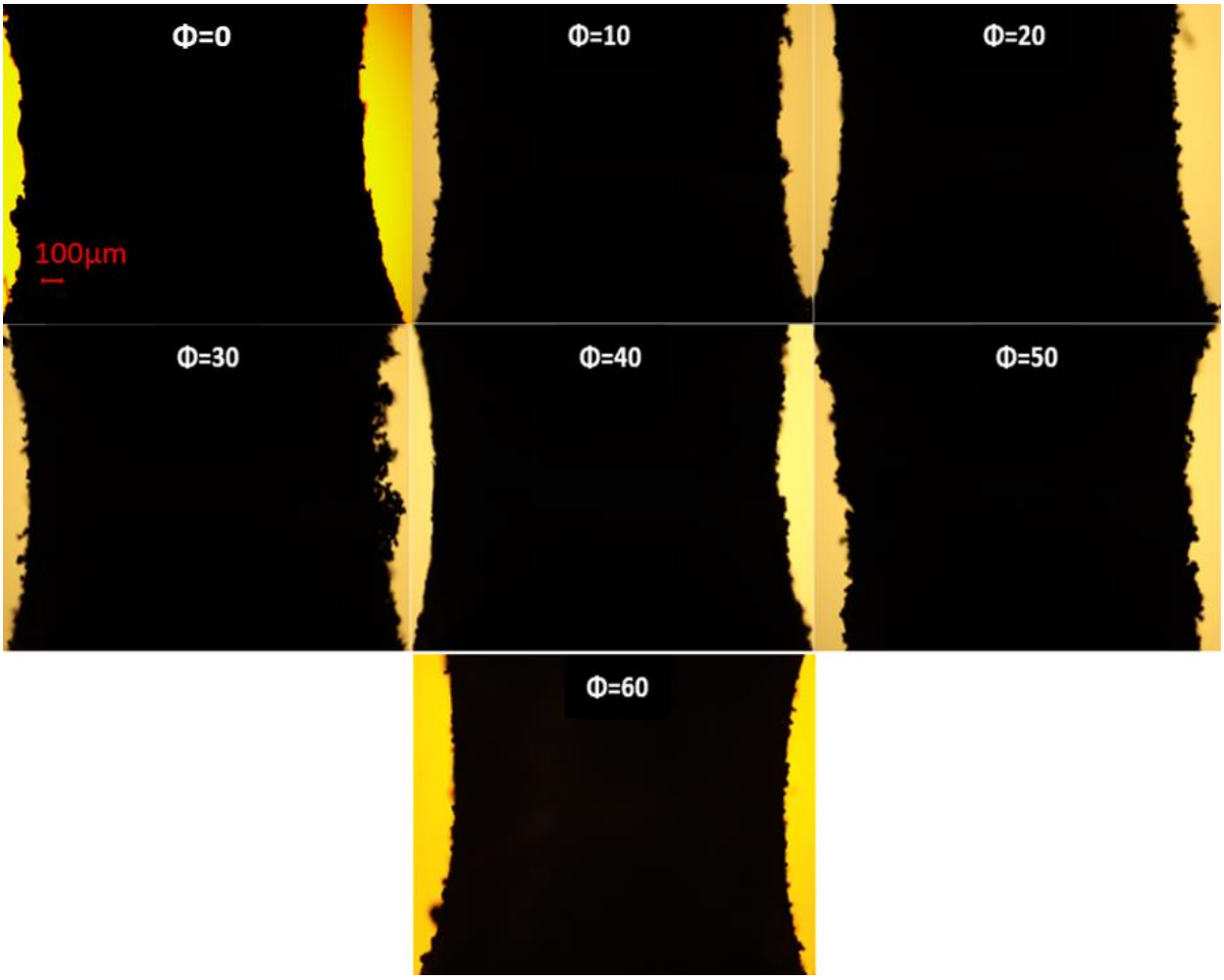

Figure 6. Microscopy images (side views) of the partially melted metal beads present along the sides of Pillar 1 on each specimen.

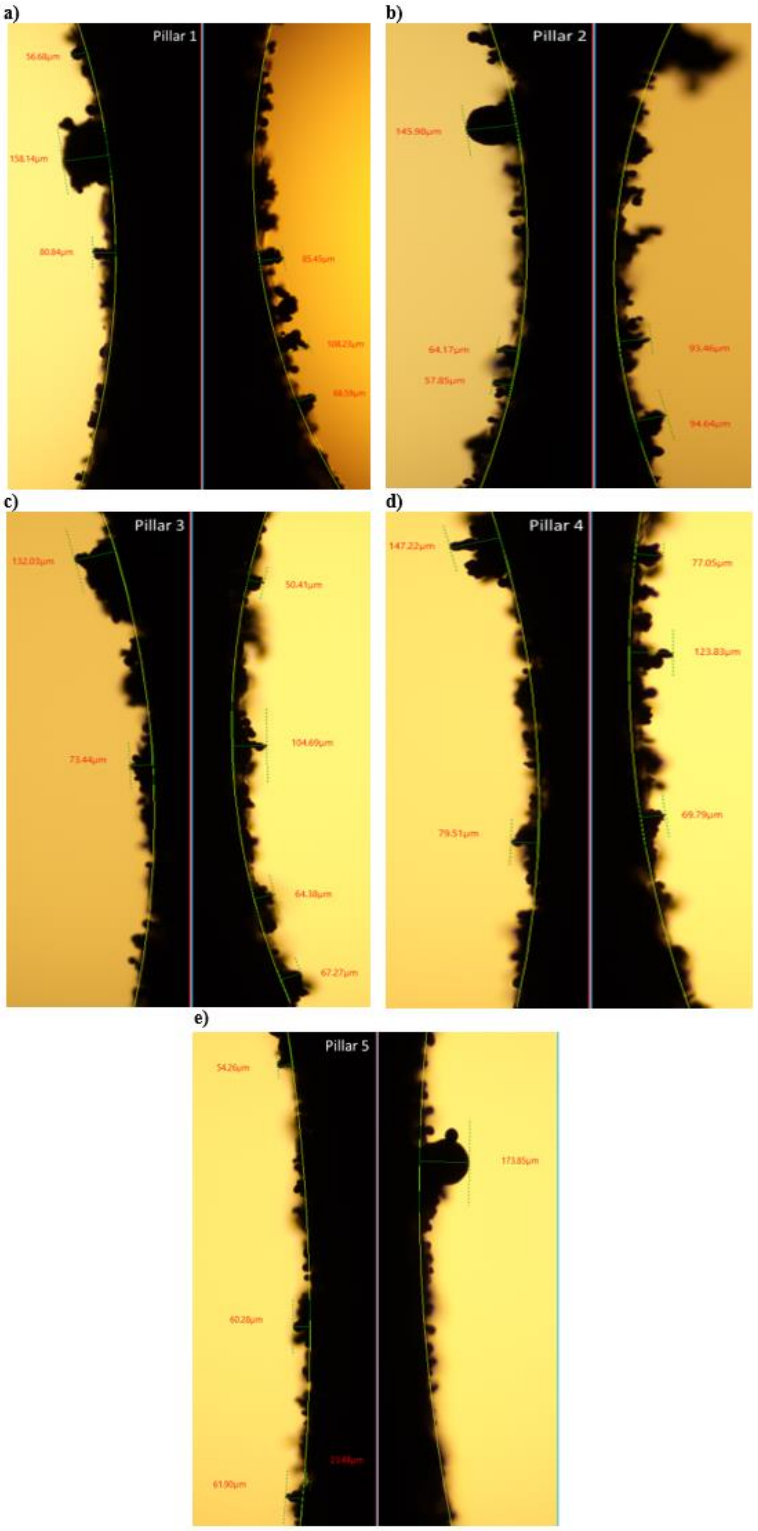

Figure 7. Microscopy images (side views) of pillar chamfer on specimen 1 (ϕ=0). Note that Pillar 1 has a chamfer angle of 30°, Pillar 2 = 25°, Pillar 3 = 20°, Pillar 4 = 15°, and Pillar 5 = 10°. Partially melted metal beads are present in large quantities on all chamfer sizes.

In Fig. 6, the shared downskin/upskin sides of Pillar 1 are visible. These are the sides that are visualized when looking directly at an upskin or downskin. It is interesting to note that the shared downskin/upskin sides are smoothest for the 40° and 60° build orientations, while roughest for the 30° and 50° build orientations. For Fig. 7, note that Pillar 1 has a chamfer angle of 30° and Pillar 5 has a chamfer angle of 10°, with each pillar chamfer angle in between varying by 5° (see Fig. 1a). From Fig. 7, it may be seen that partially-sintered beam widths varied from ~20 μm to as high as 174 μm. Agglomerations of powder with satellites are evidenced in Fig. 7a and 7d-e indicating that the chamber angle had little-to-no influence on agglomeration. There is no clear trend between pillar chamfer angle and surface roughness. However, it does appear that the steepest chamfer angle of 10° provided for the smoothest surface with the exemption of the lone agglomeration along its right side. All other chamfer angles provided for pillars with profound agglomeration – more pronounced and sporadic than that observed for Pillar 5 (10° chamfer angle).

The flat upskin surface (non-pillared) of each part was observed from two different angles, from the side and from the top, (Fig. 8 and Fig. 9). There was a trend in partially melted bead size; as the printing angle increased, the bead size generally decreased. Partially melted beads were most prominent for low build angles and diameters reduced with increasing build angle. This, in the context of how the specimens were printed, makes sense as the effect of gravity would pull these beads to the side, rather than leave them standing upright [43]. For the horizontally-printed specimen, the flat upskin was found to have one of the largest attached particles in this study, at 234 μm. The surfaces without partially-sintered particles were found to have numerous 'mounds' indicating a some type of balling effect taking place during LPBF. Figure 9, which is a top view of the flat portion of the specimens, continues to show how gravity perpendicularity affects the LPBF melt pool and subsequent surface features. Surface roughness variability, as well as a few

partially melted metal beads which have formed because of the AM process, can be seen in these figures. The flat surface of specimen 5 (ϕ=40) was the smoothest. It had the smallest difference in height and had relatively fewer partially melted metal beads. This corresponds directly with the contact angle observed earlier and explains the trend in increasing water repellency as the printing angle approached 40°. Parallel track lines are visible in Fig. 9; however, they become less apparent as the build angle increases, especially for those greater than 40°. The white and yellow streaks present in Figs. 8-9 are the result of the lighting required to obtain high resolution images of the specimens.

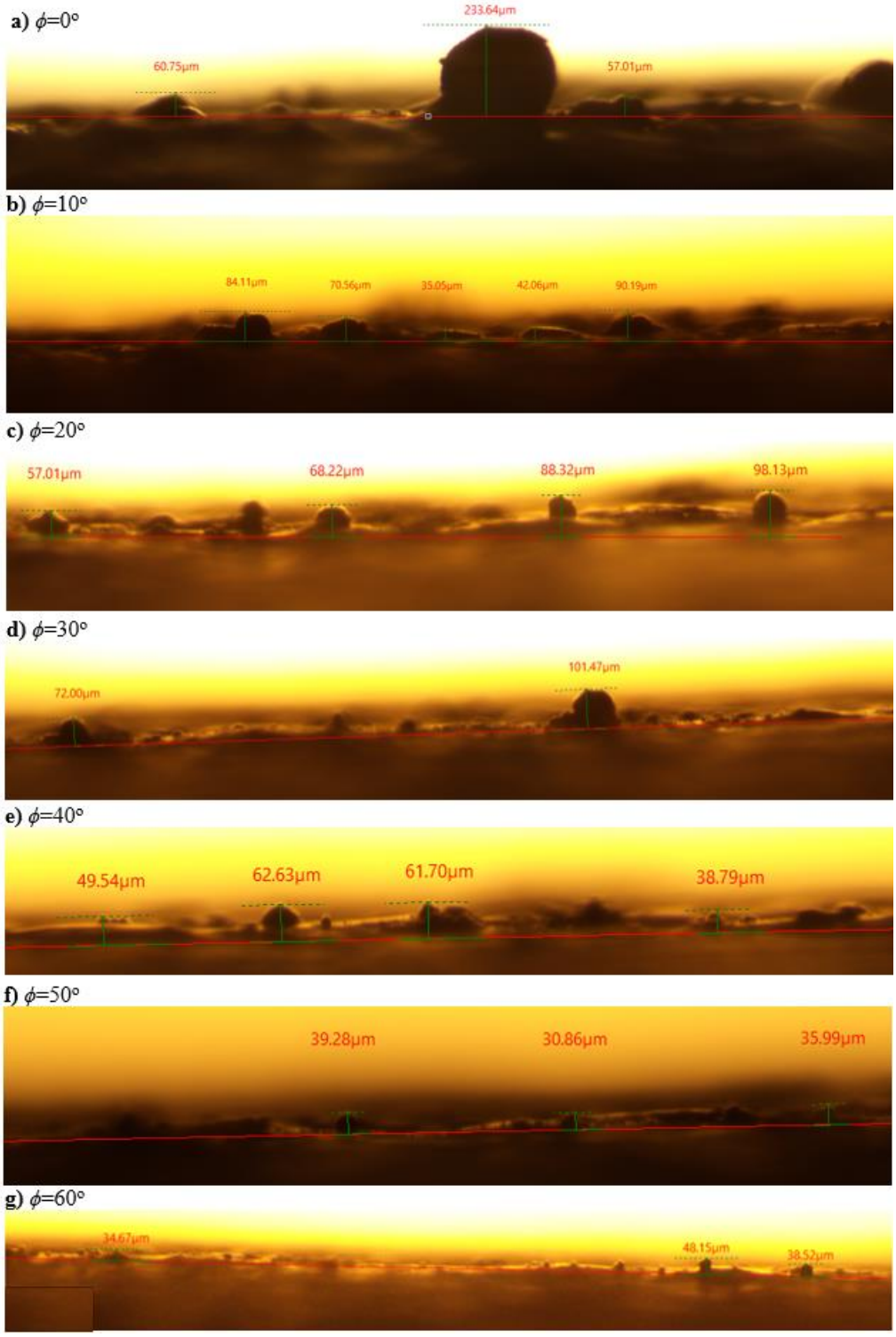

Figure 8. Side-view microscopy images of the flat upskin portion of each specimen.

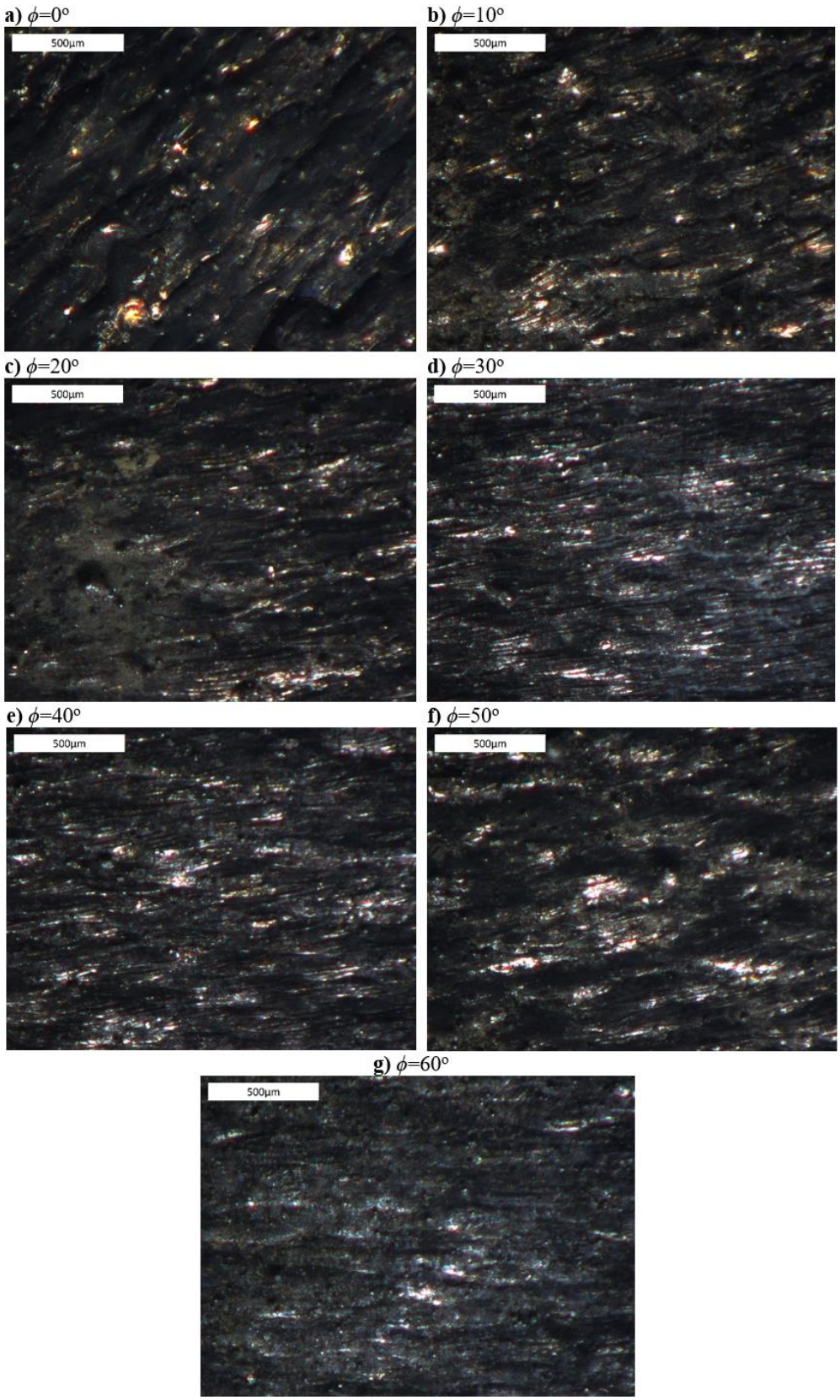

Figure 9. Optical microscope images (aerial view) of the flat upskin portion of each specimen.

Profilometer measurements

As shown in Fig. 10, profilometer measurements were performed to obtain five average roughness values, R_a, along various locations of the specimens. One measurement was obtained from the flat upskin portion of the part in the same location that the contact angle measurements were previously obtained (Fig. 11) and four measurements were obtained along the sides of the pillars (Fig. 12). The pillar roughness measurements were taken on both the left and right sides of the pillar corresponding to their upskins and downskins during LPBF, respectively. Note the evidence of localized burning along the pillar shown in Fig. 10 occurring along a shared upskin/downskin side.

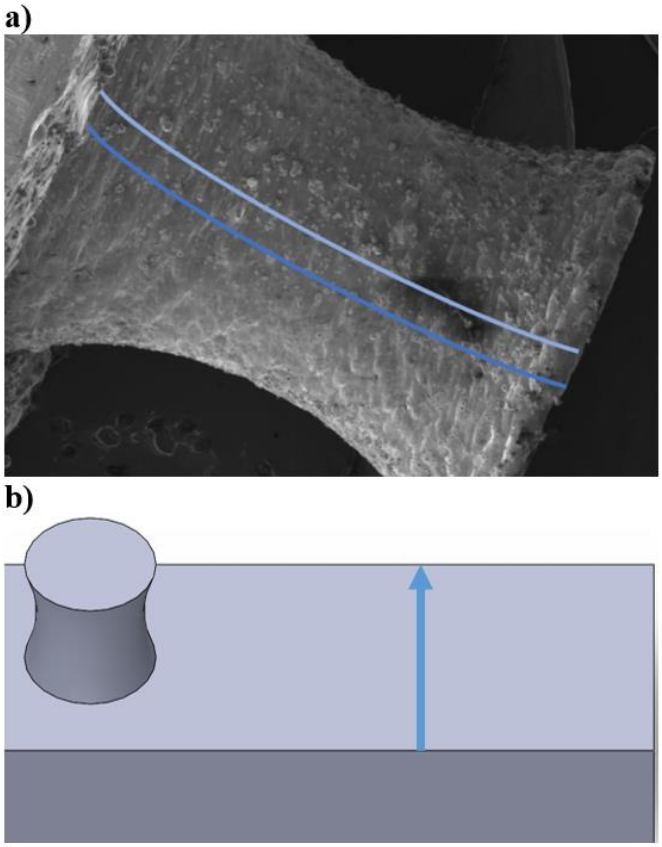

Figure 10. Location of profilometer measurement path to determine a) average roughness for the right side of the pillar (dark blue line) and a defect on the left side of the pillar (light blue line) b) average roughness for the top surface.

As shown in Fig. 10, the upskin profilometer measurements were averaged over a path 8.25 mm in length while the pillar profilometer measurements were averaged over a path 4.15 mm in length along their height. From Fig. 11, the upskin (left side) surface of each pillar was found to possess average roughness values between 8.04-12.4 μm whereas the downskin (right side) surface had average roughness values between 9.25-17.6 μm. The upskin and downskin surface roughness's of the investigated pillars clearly depend on build angle. In all cases, and as expected, the upskin surface of the pillar was smoother than its downskin surface. This is attributed to the downskin being surrounded by unmelted powder which acts as a thermal insulator and wicking medium, causing the melt pool to run hotter and be 'pulled' upon, respectively. The upskin has the advantage of having solid metal beneath it to help conduct heat away. In addition, the gravity force depresses the melt pool more due to the underlying solid preventing any permeation, generally resulting in smoother profiles. Significantly more variance in roughness was found for the pillar downskin relative to its upskin. A maximum roughness near 18 μm was measured for the pillar downskin on the 50°-built specimen. The 0°, 10°, and 60°-built specimens possessed pillars with downskin roughness values between 12-14 μm. The smoothest pillar downskins were found for the 20°, 30°, and 40°-built specimens, ranging between 9-12 μm. The upskin surface roughness values of the pillar generally increased with specimen build orientation. The upskin surface was smoothest for the 0° and 10° build orientations with values near 7-8 μm. The results demonstrate an inflection point in upskin and downskin surface roughness values – occurring around a specimen build orientation of 50°. The upskin surface roughness of the specimen flat region was highest for the 0° build orientation (~16.5 μm) and generally became smoother as the build orientation increased, being approximately 5 μm at the 60° build orientation. The trend is broken for the 50° build orientation, in which the upskin surface roughness of the specimen's flat region

is higher than that for the 40° build orientation. The upskin surface roughness barely changed for build orientations between 20° and 40°.

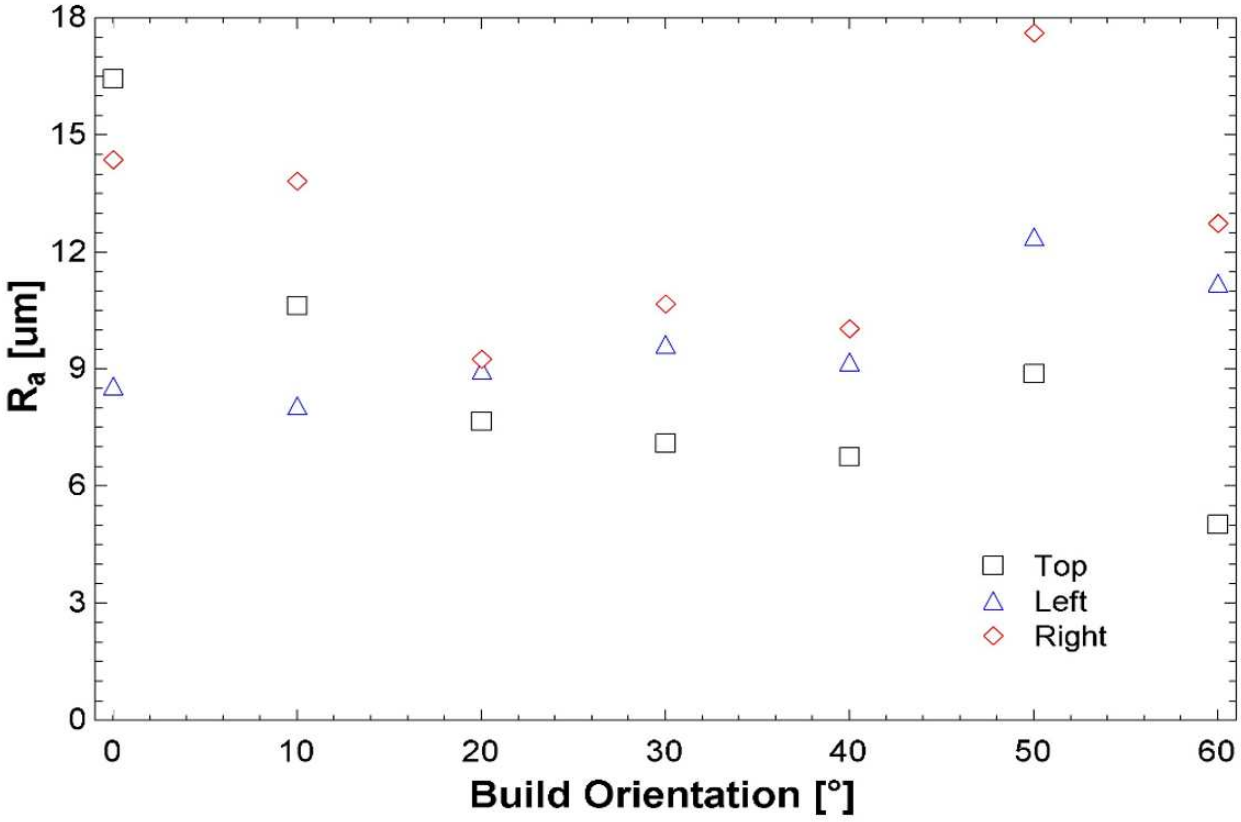

Figure 11. Average roughness of the top horizontal surface and the right and left sides of the pillar for each build orientation.

The roughness values for notable partially-attached beads (defects) on the upskin (left) and downskin (right) portions of the investigated pillar are shown in Fig. 12. It may be seen that there is strong variance in defect roughness, ranging between 11-38 μm for the pillar upskin and 12-27 μm for the pillar downskin. The defect roughness appears to have no relationship with build orientation due to the random powder size distribution used during LPBF. The variance in defect roughness is less for the pillar downskin and this may be attributed to powder bed capillary effects.

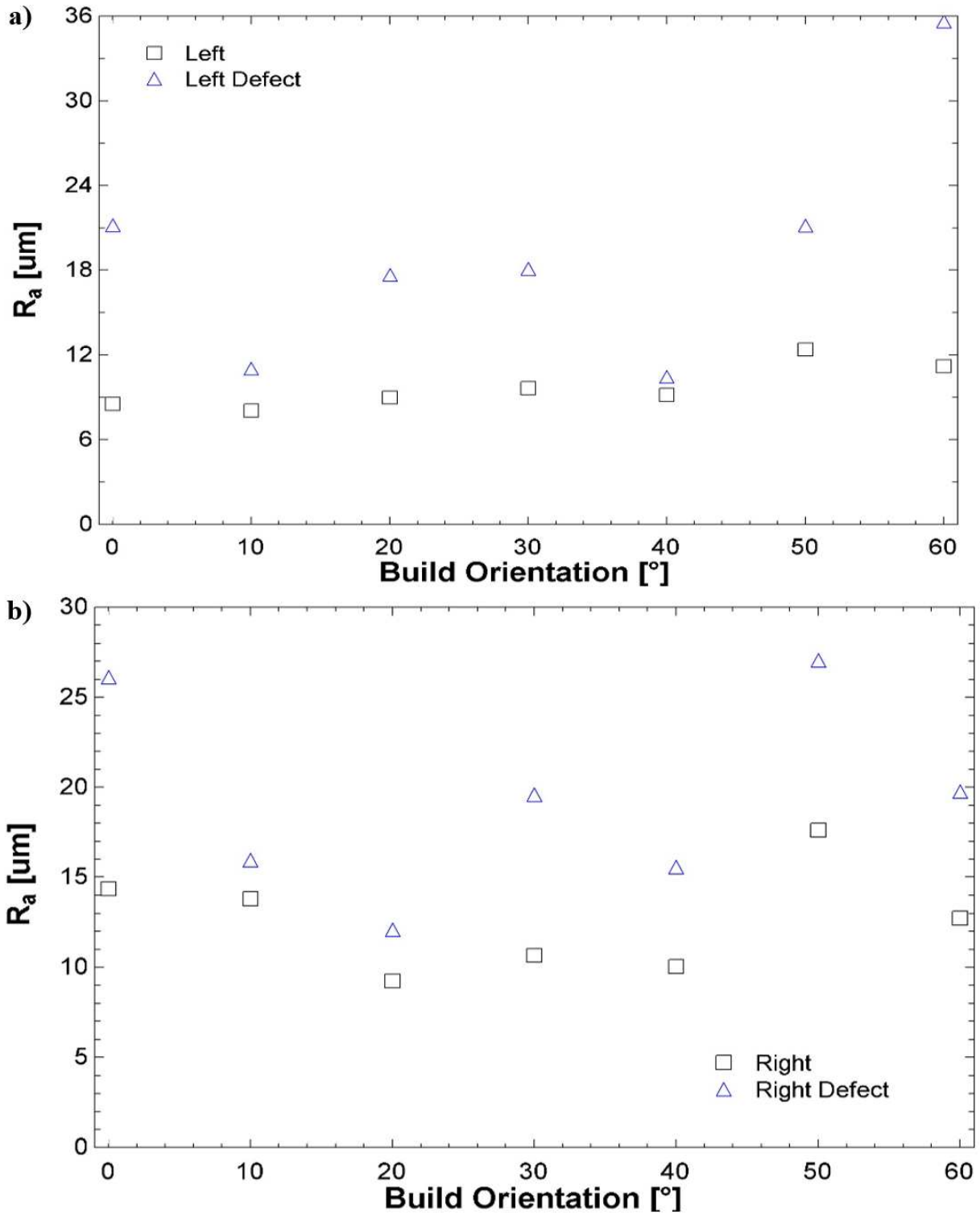

Figure 12. Average roughness for the a) left side of the pillar and a defect on the left side of the pillar b) right side of the pillar and a defect on the right side of the pillar for each build orientation.

3D Confocal Microscopy

In contrast to engineered surfaces with structured hierarchical features – shown to create superhydrophobicity [44, 45] – the laser -manufactured parts show strong anisotropy and lack a periodic structure. A Leica confocal microscope (DVM2500 Digital Microscope) was used to obtain 3D topographies (Fig. 14) at the same location contact angles were measured (Fig. 4d). Topographical images were acquired by taking a montage image of the surface and importing these images into Leica Map Start, where the 3D topographical surface views were created and arithmetic mean height, *Sa*, areal material ratio, *Smr*, and inverse areal material ratio, *Smc*, were computed. Arithmetic mean height expands roughness from a line (i.e., *Ra*) to a surface according to ISO 25178. Arithmetic mean height, given in microns in Fig. 14, is presented for the seven build angles, and its relationship with measured contact angles is shown in Fig. 15. For the 0.2-μL droplets utilized in these experiments, nominal droplet diameters were calculated. On a flat surface, the droplet diameter is dependent on droplet volume, V, and contact angle, θ, according to the following geometric relationship [46],

$$D = \left(\frac{24V}{\pi}\left(\frac{sin^3\,\theta}{2-3\,cos\theta+cos^3\,\theta}\right)\right)^{1/3} \tag{4}$$

The non-dimensional Bond number, Bo, represents the importance of gravitational forces to surface tension forces,

$$Bo = \frac{\rho g r^2}{\sigma_{LV}} \tag{5}$$

where ρ is density, g is local gravitational acceleration, r is droplet radius, and σ is surface tension. For Bo<1, surface tension forces dominate, and droplet shape's dependence on gravity is negligible [47]. For the 0.2 μL droplet studied in the manuscript, as well as ± 40%, the resultant

Bond numbers are significantly under 1. Therefore, the droplet shape and resultant contact angles are not sensitive to variance in droplet volume.

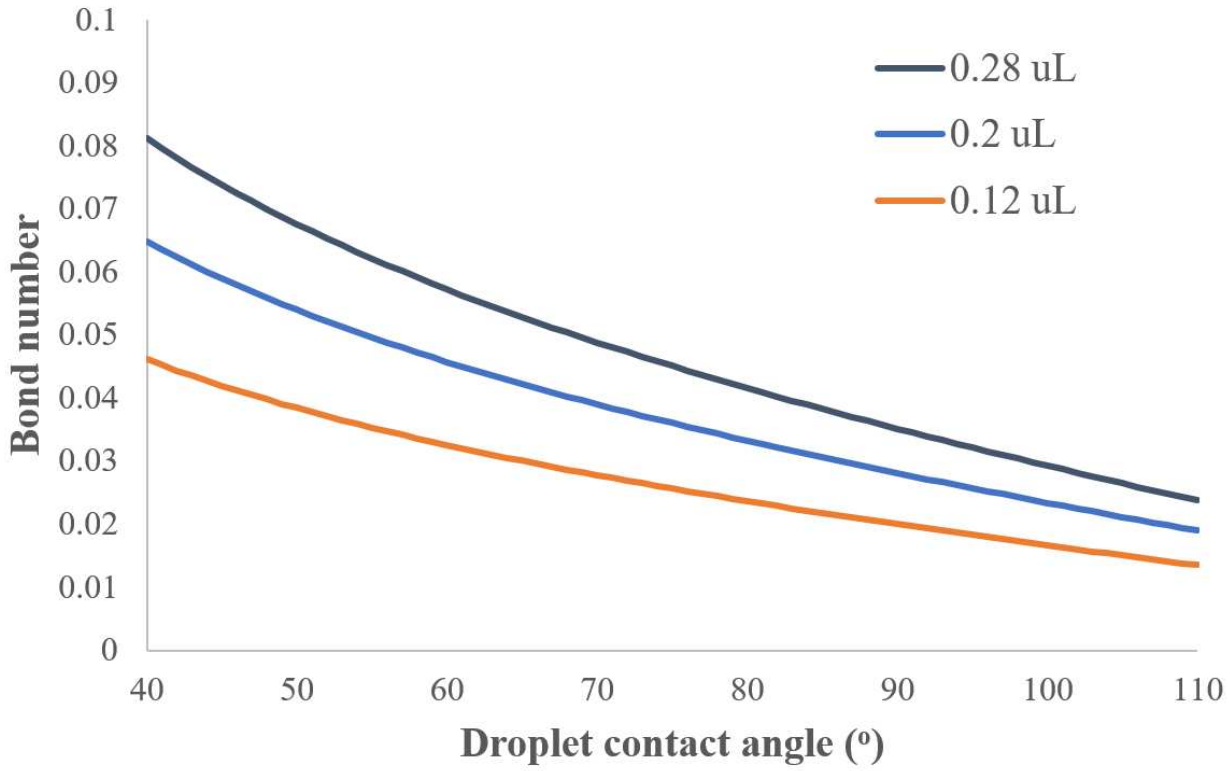

Figure 13. Droplet contact angles and their corresponding bond numbers for 0.2 µL ± 40% droplets.

A nominal diameter of 1.38 mm was obtained for a contact angle of 40°, and a diameter of 0.75 mm for a contact angle of 110°; compared to the roughness, maximum peaks of 204 µm were observed on the surface with a build angle of 50°. Roughness impacts wettability. According to the classic theory by Wenzel, for wetting surface (i.e., θ<90°), increased roughness increases hydrophilicity, while for non-wetting θ>90°, increased roughness increases hydrophobicity [48]. In this work, the contact angle of 90° distinguishes between the hydrophobic and hydrophilic regimes and the AlSi10Mg surface is hydrophobic by nature [19], so according to classic Wenzel theory, hydrophobicity should be observed. However, Wenzel's theory does not adequately predict

behavior for anisotropic rough surfaces. Plawsky et al. [49] notes that a sessile liquid droplet placed on a rough surface may not be in either a Wenzel state (i.e., liquid fully penetrates roughness) or Cassie Baxter state (i.e., air pockets in the roughness support the droplet). Droplet behavior depends on the interaction between the liquid and rough surface. Liquid may partially imbibe in the rough surface, and droplets on the size of the roughness may have varying contact angles around the droplet's perimeter. Huang and Gates [50] observed 5-μL water droplets on rough surfaces (e.g., hydrophobic sand, glass beads, and a combination of particles). Contact angles varied based on the perimeter in contact with the rough surface.

The LPBF process results in heterogeneous surfaces, as demonstrated by the partially melted beads shown in Figure 8, microscopy images presented in Figures 7, 9 and 10, and the surface characterizations in Figures 14 and 15. Wetting behavior depends on the surface energy of the material, nano- and micro-scale structures, and periodicity of the structures [51-56]. Natural superhydrophobic surfaces such as butterfly wings rely on asymmetric micro- or nano-structures, thereby resulting in anisotropic wetting [51]. Engineered surfaces can also promote anisotropic wetting. Wang et al. [52] investigated wetting on hydrophilic and hydrophobic stripe patterns, observed non-hemispherical equilibrium droplet shapes, and noted "the anisotropic wetting makes Cassie−Baxter theory no longer applicable globally." Similarly, Vrancken et al [53]. investigated wetting on polygonal posts which resulted in polygonal shaped droplets. They expressed the importance of the lattice arrangement and shapes of the posts in dictating anisotropic wetting.

The results in Figures 14 and 15 indicate that the lack of periodic structures (e.g., partially melted beads observed in Figure 8) of the LPBF-manufactured surfaces impacts wetting, and can lead to anisotropic wetting (i.e., hydrophilic and hydrophobic behavior in the same droplet). The build angle of 0^{o} has one of the highest values of *Sa* and *Sdr,* and also corresponds to the differing

contact angle behavior, with most contact angles hydrophilic, yet one droplet experiences anisotropic wetting, in which the left side of the droplet is hydrophilic (i.e., θ=81.7^{o}) and hydrophobic on the right side (i.e., θ=93.6^{o}). Arithmetic mean heights and developed interfacial area ratios are the lowest for build angles of 30^{o} and 40^{o}, which maintain their hydrophobicity for all tested droplets, indicating that the more consistent surface roughness may be responsible for the hydrophobic contact angles. Belaud et al. [54] noted that although *r*, the roughness parameter pertaining to the Wenzel wetting state, is related to *Sdr*, the developed interfacial area ratios were very sensitive to micro-cavities, for their experiments using polypropylene textured using a femtosecond laser, the droplets were in neither Cassie-Baxter nor Wenzel modes.

Zhou et al. [55] explored laser remelting in order to improve the surface quality of LPBF-manufactured parts. In an AlSi10Mg sample, the initial sample displayed 70° contact angles; following laser remelting, the surface quality improved, and contact angle increased to 89°. They observed similar values of *Sa*, 17 μm on the top surface, comparable to the 15.52-21.71 μm observed in this study, although their side values of *Sa* (i.e., 6.5 μm) are lower than those observed in this study. However, the authors did not report nor consider the impacts of build angle in their study, as the study focused on improving surface quality.

a) ϕ=0º

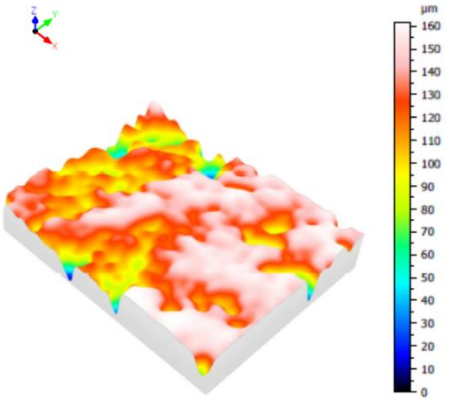

b) ϕ=10º

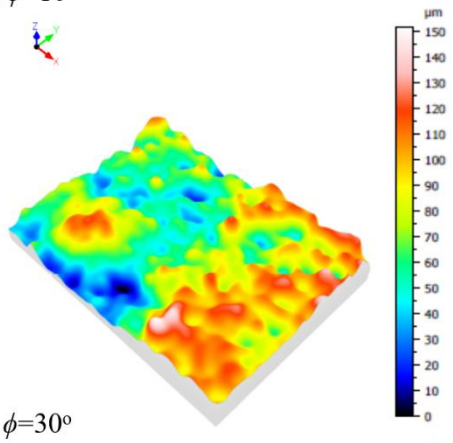

c) ϕ=20º

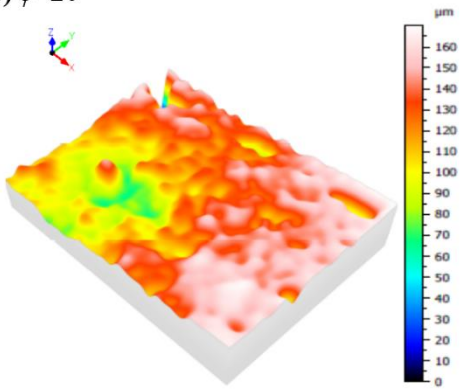

d) ϕ=30º

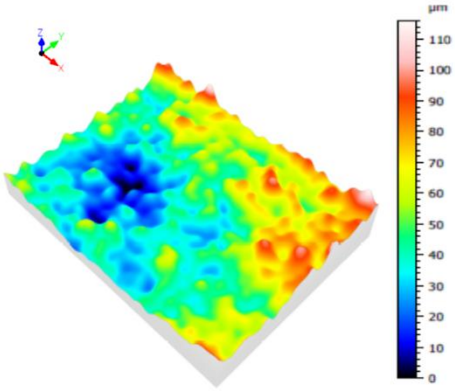

e) ϕ=40º

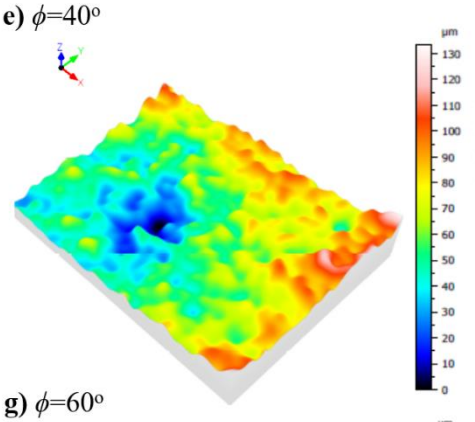

f) ϕ=50º

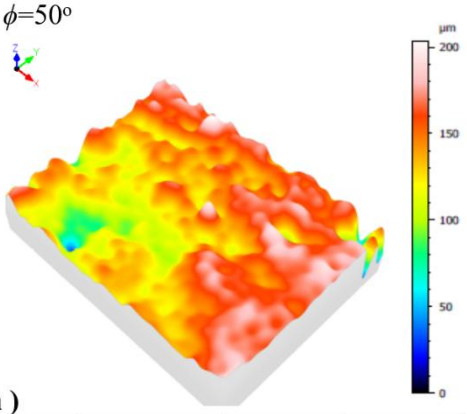

g) ϕ=60º

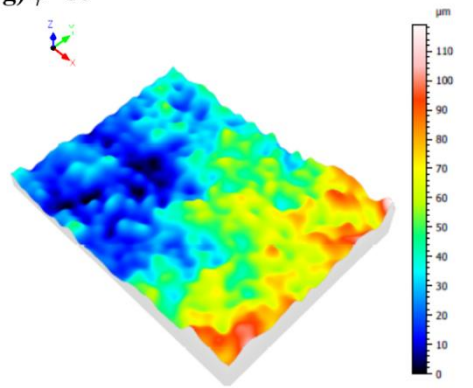

h)

Build angle (º)	Arithmetic mean height, Sa (um)	Areal material ratio, Smr (%)	Inverse areal material ratio (um)	Developed interfacial area ratio (Sdr) (%)
0º	20.99	0.727	29.186	9.66
10º	21.71	0.00964	34.047	6.57
20º	20.12	0.05347	29.159	5.55
30º	15.52	0.00345	26.244	3.12
40º	16.84	0.00169	27.214	3.21
50º	20.55	0.02234	31.447	7.75
60º	18.45	0.00384	30.661	2.48

Figure 14. Topographical maps corresponding to location from Figure 4d, with build angles, ϕ, of a) 0º, b) 10º, c) 20º, d) 30º, e) 40º, f) 50º, and g) 60º; h) ISO 25178 parameters for all build angles, including arithmetic mean height *Sa*, areal material ratio, *Smr*, inverse areal material ratio, and developed interfacial area radio, *Sdr*.

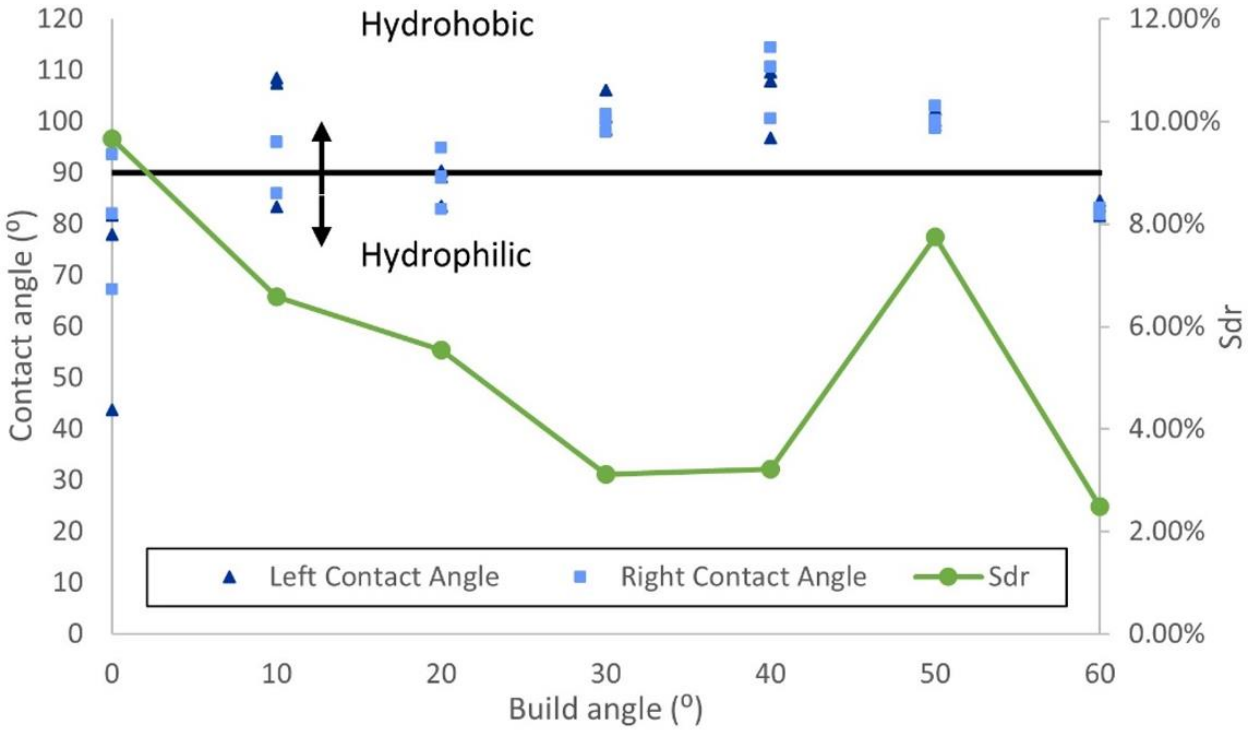

Figure 15. Droplet contact angles and developed interfacial area ratio as a function of build angle; arithmetic mean heights are one indicator of anisotropy in surface roughness.

From Figure 15, it may be seen that the Sdr decreases steadily with build angle until 30°. From 30° to 40° the Sdr does not change significantly; however, the Sdr increases abruptly when going from a build angle of 40° to 50°. Then, from 50° to 60°, the Sdr decreases to a value less than that measured for the 40° angle. This trend suggests there is a critical build angle between 40° and 50° with regards to Sdr. This spike in surface roughness at 40º-50º build orientation was demonstrated to a similar extent by Hovig et al. [57] for the LPBF of AlSi10Mg flat tensile

specimens. They show a clear jump in surface roughness when going from a 30º build angle to a 45º build angle. Then, a decrease in surface roughness was observed for all angles greater than 60º. A similar spike in surface roughness was also observed, although to a lesser extent, by Karlsson et al. [58]. In their study, they investigated LPBF tool steel and the surface roughness was shown to decrease rapidly with build angle, but when going from a build angle of 40º to 45º a flat trend resulted, while all other changes in build orientation provided for a marked decrease in roughness. Interestingly, Ullah et al. [59] found a steadily decreasing trend in surface roughness along the upskin of LPBF AlSi10Mg flat plates with increasing build angles. Based on there being some inconsistency between various studies (including this one), it is not clear what the mechanism is for the sudden increase in surface roughness around the 50º build angle. Any criticality in surface roughness with respect to build angle would have to depend on the permeability of the powder bed and its resulting capillary force on the melt pool during the contour track melting. With the help of gravity, the capillary force would have to be great enough to pull sufficiently against frictional and surface tension forces of the melt pool. The result would be higher surface roughness due to partial wicking followed by solidification. There is a critical contact angle in which maximum wicking occurs for a fluid amongst a three-dimensional compact bed of spheres [60-61]. This critical contact angle is ~51º and it is interesting to note that this is very close to the build angles in which surface roughness is maximum. This means that when/if the melt pool achieves a contact angle of ~51º the capillary force becomes maximized. It is feasible to assume that molten AlSi10Mg can achieve such a contact angle while co-existing with its solid phase as similar contact angles have been reported in the literature [62]. In all cases, heterogeneities in the LPBF-manufactured components resulted in anisotropic wetting. Since the heterogeneities are defects of the manufacturing process, they do not exhibit uniform size nor spacing, thereby

resulting in anisotropic wetting influenced by the part's build angle. Vapor chamber designers should be aware of the anisotropy in LPBF-manufactured surfaces impacting wettability.

Conclusions

Trends of water contact angles on AlSi10Mg surfaces manufactured via LPBF at various build orientations were investigated. Several qualitative and quantitative measurements have been provided. Although the powdered AlSi10Mg alloy is typically hydrophobic, wettability varied based on build angle: build angles of 0˚ and 60˚ exhibited primarily hydrophilic behavior, build angles of 10˚ and 20˚ demonstrated a mix of hydrophobic and hydrophilic behavior, and hydrophobic behavior was observed for 30˚, 40˚, and 50˚ build angles. The build/printing angle affects the roughness of the surface as well as the size and number of partially melted metal beads formed due to gravitational and powder-bed-capillary effects during the LPBF process. It was determined that the surfaces printed at 30º and 40˚ printing angles had the smoothest overall surfaces and, therefore, the highest solid-liquid contact angles (i.e., consistently hydrophobic). Surfaces were not homogenous and measured surface roughness, *Ra*, ranged from 5-36 μm, and arithmetic mean heights, *Sa*, ranged from 15.52-21.71 μm with variations based on location. The size of the partially melted metal beads decreased as the printing orientation angle increased. This information will be used in further experiments to determine the desired printing angle of VCs. A significantly rougher surface was found for the 50º build angle. Based on the theoretical capillary behavior of a fluid with a compact bed of spheres, a critical contact angle of 51º results in the melt pool permeating the powder bed at a maximum. The critical melt pool contact angle and build angle in this case are near equal suggesting a critical build angle exists which gives rise to pronounced melt pool wetting behavior and increased surface roughness due to partial wicking

followed by solidification. Based on this study, the effects of the printing angle did not conclusively change the surface roughness of different shaped geometries due to strong anisotropy in roughness observed. Due to the nature of LPBF, as well as the process factors used to produce the specimens of this study, the surface of the specimens contained significant mini-structures which may prove valuable in the aid of heat transfer and bubble formation in VCs.

Acknowledgements

JAM, EMSC, and MMD gratefully acknowledge the support of NSF Grant #1828571.

References

[1] Ma, H., 2016, Oscillating Heat Pipes. Springer Science + Business Media New York 2015, pp. 389.

[2] Davoud Jafari, Wessel W. Wits, Bernard J. Geurts, Phase change heat transfer characteristics of an additively manufactured wick for heat pipe applications, *Applied Thermal Engineering*, Vol. 168, 2020, 114890.

[3] Thompson, Scott & Ma, Hongbin. Recent Advances in Two-Phase Thermal Ground Planes. *Annual Review of Heat Transfer*, 2015, 2015011163.

[4] Zhao, C., Fezzaa, K., Cunningham, R.W. et al. Real-time monitoring of laser powder bed fusion process using high-speed X-ray imaging and diffraction. *Sci Rep 7, 3602,* 2017.

[5] Bailey, Christopher M. Weeks, Cameron. Thompson, Scott M. “Design and Performance of a Novel AlSi10Mg Vapor Chamber Fabricated via Laser Powder Bed Fusion” Solid Freeform Fabrication Conference. Paper 63599: Virtual Event, August 2-4, 2021.

[6] ASTM Standard 52900:E, 2015, “Standard Terminology for Additive Manufacturing -General Principles- Terminology,” ASTM International, West Conshohocken, PA, 2016.

[7] Gibson, Ian, David Rosen, and B. Stucker. *Additive Manufacturing Technologies: 3d Printing, Rapid Prototyping, and Direct Digital Manufacturing*. Springer Verlag, 2016.

[8] Gennaro Salvatore Ponticelli, Oliviero Giannini, Stefano Guarino, Matthias Horn, An optimal fuzzy decision-making approach for laser powder bed fusion of AlSi10Mg alloy, *Journal of Manufacturing Processes*, Vol. 58, 2020, pp. 712-723.

[8a] Tian, Q., Guo, S., Melder, E., Bian, L., and Guo, W. “. (December 17, 2020). "Deep Learning-Based Data Fusion Method for In Situ Porosity Detection in Laser-Based Additive Manufacturing." ASME. J. Manuf. Sci. Eng. April 2021; 143(4): 041011.

[8b] Ramesh Sagar, V., Lorin, S., Wärmefjord, K., and Söderberg, R. (March 5, 2021). "A Robust Design Perspective on Factors Influencing Geometric Quality in Metal Additive Manufacturing." ASME. J. Manuf. Sci. Eng. July 2021; 143(7): 071011. https://doi.org/10.1115/1.4048742

[9] A. du Plessis, S. Beretta, Killer notches: The effect of as-built surface roughness on fatigue failure in AlSi10Mg produced by laser powder bed fusion, *Additive Manufacturing*, Vol. 35, 2020, 101424.

[10] Wangyu Liu, Yi Peng, Tao Luo, Yuanqiang Luo, Kaidong Huang, The performance of the vapor chamber based on the plant leaf, *International Journal of Heat and Mass Transfer*, Vol. 98, 2016, pp. 746-757.

[11] Esarte, J., Blanco, J., Bernardini, A., & San-José, J. (2017). Optimizing the design of a two-phase cooling system loop heat pipe: Wick manufacturing with the 3D selective laser melting printing technique and prototype testing. *Applied Thermal Engineering*, Vol. 111, 2016, pp. 407-419.

[12] Jafari, D., Wits, W. W., & Geurts, B. J. (2017). An investigation of porous structure characteristics of heat pipes made by additive manufacturing. Paper presented at the 2017 23rd International Workshop on Thermal Investigations of ICs and Systems (THERMINIC).

[13] Jafari, D., Wits, W. W., & Geurts, B. J. (2018). Metal 3D-printed wick structures for heat pipe application: Capillary performance analysis. *Applied Thermal Engineering*, Vol. 143, 2018, pp. 403-414.

[14] Hadley Brooks, Kevin Brigden, Design of conformal cooling layers with self-supporting lattices for additively manufactured tooling, *Additive Manufacturing*, Vol. 11, 2016, pp. 16-22.

[15] Scott M. Thompson, Zachary S. Aspin, Nima Shamsaei, Alaa Elwany, Linkan Bian, Additive manufacturing of heat exchangers: A case study on a multi-layered Ti–6Al–4V oscillating heat pipe, *Additive Manufacturing*, Vol. 8, 2015, pp. 163-174.

[16] Du, Y., & Tong, P. Turbulent thermal convection in a cell with ordered rough boundaries, *Journal of Fluid Mechanics*, Vol. 407, 2000, pp. 57-84.

[17] S. M. Demsky & H. B. Ma. “Thin film evaporation on a curved surface.”, *Microscale Thermophysical Engineering*, pp. 285-299, 2004.

[18] Chi Young Lee, Wang Kee In. Prediction of water droplet evaporation on zircaloy surface, *Journal of Nuclear Science and Technology*, Vol. 51:4, 2014, pp. 448-456.

[19] Fathi, Parisa & Mohammadi, Mahyar & Nasiri, A. Low Surface Roughness Additively Manufactured AlSi10Mg: *The Impacts on Corrosion and Water Repellency Properties*. 2020, pp. 209-320.

[20] Chen, Xi; Derby, Melanie M. Combined Visualization and Heat Transfer Measurements for Steam Flow Condensation in Hydrophilic and Hydrophobic Mini-Gaps, *Journal of Heat Transfer*, Vol. 138, 2016.

[21] Bachir El Fil, Girish Kini, Srinivas Garimella. A review of dropwise condensation: Theory, modeling, experiments, and applications." *International Journal of Heat and Mass Transfer* Vol. 160, 2020.

[22] Attinger, D., Frankiewicz, C., Betz, A., Schutzius, T., Ganguly, R., Das, A., Chang-Jin, K., Megaridis, C. Surface engineering for phase change heat transfer: A review. *MRS Energy & Sustainability*, Vol. 1, 2014.

[22a] Snyder, J. C., and Thole, K. A. (May 6, 2020). "Understanding Laser Powder Bed Fusion Surface Roughness." ASME. J. Manuf. Sci. Eng. July 2020; 142(7): 071003. https://doi.org/10.1115/1.4046504

[23] Mohammad Montazeri & Prahalada Rao. Sensor-Based Build Condition Monitoring in Laser Powder Bed Fusion Additive Manufacturing Process Using a Spectral Graph Theoretic Approach, *Journal of Manufacturing Science and Engineering*, Vol. 140, 2018.

[24] Slegers, Sam & Linzas, Mathias & Drijkoningen, Jeroen & D'Haen, Jan & Reddy, Naveen & Deferme, Wim. Surface Roughness Reduction of Additive Manufactured Products by Applying a Functional Coating Using Ultrasonic Spray Coating. *Coatings*. Vol. 7, 2017.

[25] Tao Yang, Tingting Liu, Wenhe Liao, Eric MacDonald, Huiliang Wei, Xiangyuan Chen, Liyi Jiang, The influence of process parameters on vertical surface roughness of the AlSi10Mg parts fabricated by selective laser melting, *Journal of Materials Processing Technology*, Vol. 266, 2019, pp. 26-36.

[26] Wenhui Yu, Swee Leong Sing, Chee Kai Chua, Xuelei Tian, Influence of re-melting on surface roughness and porosity of AlSi10Mg parts fabricated by selective laser melting, *Journal of Alloys and Compounds*, Vol. 792, 2019, pp. 574-581.

[27] Kuisat, Florian et al. "Simultaneous Micro-Structuring and Surface Smoothing of Additive Manufactured Parts Using DLIP Technique and Its Influence on the Wetting Behaviour." *Materials (Basel, Switzerland),* Vol. 14(10), 2021.

[28] Ali Davoudinejad, Yukui Cai, David Bue Pedersen, Xichun Luo, Guido Tosello, Fabrication of micro-structured surfaces by additive manufacturing, with simulation of dynamic contact angle, *Materials & Design*, Vol. 176, 2019.

[29] Gogolewski, D., Bartkowiak, T., Kozior, T., Zmarzły, P. "Multiscale Analysis of Surface Texture Quality of Models Manufactured by Laser Powder-Bed Fusion Technology and Machining from 316L Steel." *Materials*, 14, 2794, 2021.

[30] Snyder, J. C., and Thole, K. A. (May 6, 2020). "Understanding laser powder bed fusion surface roughness." ASME. *J. Manuf. Sci. Eng*. Vol.142(7), July 2020

[31] Leis A, Weber R, Graf T. Process Window for Highly Efficient Laser-Based Powder Bed Fusion of AlSi10Mg with Reduced Pore Formation. *Materials (Basel)*, Vol 14, 2021.

[32] Li, Bao-Qiang & Li, Zhonghua & Bai, Peikang & Liu, Bin & Kuai, Zezhou. Research on Surface Roughness of AlSi10Mg Parts Fabricated by Laser Powder Bed Fusion. *Metals*, Vol 8, 2018.

[33] Yu, W., Sing, S. L., Chua, C. K., and Tian, X. "Influence of Re-Melting on Surface Roughness and Porosity of AlSi10Mg Parts Fabricated by Selective Laser Melting." *Journal of Alloys and Compounds*, Vol. 792, pp. 574–581, 2019.

[34] Dong, Z., Liu, Y., Li, W., and Liang, J. "Orientation Dependency for Microstructure, Geometric Accuracy and Mechanical Properties of Selective Laser Melting AlSi10Mg Lattices." *Journal of Alloys and Compounds*, Vol. 791, pp. 490–500, 2019.

[35] Hofele, M. , Roth, A. , Schanz, J. , Harrison, D. , De Silva, A. and Riegel, H. Laser "Polishing of Laser Powder Bed Fusion AlSi10Mg Parts—Influence of Initial Surface Roughness on Achievable Surface Quality." *Materials Sciences and Applications*, Vol. 12, pp. 15-41, 2021.

[36] Gouveia, R.M.; Silva, F.J.G.; Atzeni, E.; Sormaz, D.; Alves, J.L.; Pereira, A.B. Effect of Scan Strategies and Use of Support Structures on Surface Quality and Hardness of L-PBF AlSi10Mg Parts. *Materials*, *13*, 2248, 2020.

[37] E.O. Olakanmi, R.F. Cochrane, K.W. Dalgarno, A review on selective laser sintering/melting (SLS/SLM) of aluminum alloy powders: Processing, microstructure, and properties, *Progress in Materials Science*, Vol. 74, 2015, pp, 401-477.

[38] Yu-Hsun Hung, Shung-Wen Kang, and Wan-Chun Tsai. "Strain analysis of vapor chamber heat spreaders." *Journal of Marine Science and Technology*. Vol 18, No. 2, pp. 277-283, 2010.

[39] Lin-zhi Wang, Sen Wang, Jiao-jiao Wu, Experimental investigation on densification behavior and surface roughness of AlSi10Mg powders produced by selective laser melting, *Optics & Laser Tech.*, Vol. 96, 2017, pp. 88-96.

[40] Tao Yang, Tingting Liu, Wenhe Liao, Eric MacDonald, Huiliang Wei, Xiangyuan Chen, Liyi Jiang, The influence of process parameters on vertical surface roughness of the AlSi10Mg parts fabricated by selective laser melting, *Journal of Materials Processing Technology*, Vol. 266, 2019, pp. 26-36.

[41] Carey, V. P. *Liquid-vapor phase-change phenomena 2nd edition*. Hemisphere. 2008, pp. 55.

[42] J M Dubois *et al*. Measurements of contact angles of water on Al-based intermetallic surfaces, *Journal of Physics: Condensed Matter*, Vol. 20, 2008.

[43] Alberto Boschetto, Luana Bottini, Francesco Veniali, Roughness modeling of AlSi10Mg parts fabricated by selective laser melting, *Journal of Materials Processing Technology*, Vol. 241, 2017, pp. 154-163.

[44] Miljkovic, Nenad, and Evelyn N. Wang. "Condensation heat transfer on superhydrophobic surfaces." *MRS bulletin* 38.5, 2013, pp. 397-406.

[45] Boreyko, Jonathan B., et al. "Wetting and dewetting transitions on hierarchical superhydrophobic surfaces." *Langmuir* 27.12, 2011, pp. 7502-7509.

[46] Sommers, Andrew, and Anthony M. Jacobi. "Calculating the volume of water droplets on topographically-modified, micro-grooved aluminum surfaces.", 2008.

[47] Bell, Michael S., Kristen A. Fichthorn, and Ali Borhan. "Effect of gravity on the configuration of droplets on two-dimensional physically patterned surfaces." Langmuir 32.16, 2016, pp. 3858-3866.

[48] Wenzel, Robert N. "Resistance of solid surfaces to wetting by water." *Industrial & Engineering Chemistry* 28.8, 1936, pp. 988-994.

[49] Plawsky, Joel L., et al. "Review of the effects of surface topography, surface chemistry, and fluid physics on evaporation at the contact line." *Chemical Engineering Communications* 196.5, 2008, pp. 658-696.

[50] Huang, X., Gates, I. Apparent Contact Angle around the Periphery of a Liquid Drop on Roughened Surfaces. *Sci Rep* 10**,** 8220 2020.

[51] Hancock, Matthew J., Koray Sekeroglu, and Melik C. Demirel. "Bioinspired directional surfaces for adhesion, wetting, and transport." *Advanced functional materials* Vol. 22.11 pp. 2223-2234, 2012.

[52] Wang, Yuxiang, et al. "Anisotropic wetting of droplets on stripe-patterned chemically heterogeneous surfaces: effect of length ratio and deposition position." *Langmuir* Vol. 35.12 pp. 4387-4396, 2018.

[53] Vrancken, Robert J., et al. "Anisotropic wetting and de-wetting of drops on substrates patterned with polygonal posts." *Soft Matter* Vol. 9.3, pp. 674-683, 2013.

[54] Belaud, Vanessa, et al. "Wettability versus roughness: Multi-scales approach." *Tribology International* Vol. 82: pp. 343-349, 2015.

[55] Zhou, Jiantao, et al. "Investigation of layer-by-layer laser remelting to improve surface quality, microstructure, and mechanical properties of laser powder bed fused AlSi10Mg alloy." *Materials & Design* Vol. 210: 2021.

[56] Kim, Tae-il, and Kahp Y. Suh. "Unidirectional wetting and spreading on stooped polymer nanohairs." *Soft Matter* Vol. 5.21, 4131-4135.

[57] Hovig, EW, Azar, AS, Sunding, MF, Andreassen, E, Sørby, K. High cycle fatigue life estimation of materials processed by laser powder bed fusion. Fatigue Fract Eng Mater Struct. 2019; 42: 1454– 1466.

[58] Jussi Karlsson et al 2021 IOP Conf. Ser.: Mater. Sci. Eng. 1135 012020

[59] Ullah, R., Akmal, J.S., Laakso, S.V.A. et al. Anisotropy of additively manufactured AlSi10Mg: threads and surface integrity. Int J Adv Manuf Technol 107, 3645–3662 (2020).

[60] P. S. Raux, H. Cockenpot, M. Ramaioli, D. Quéré, and C. Clanet. Wicking in a Powder. Langmuir 2013 29 (11), 3636-3644.

[61] Shirtcliffe,N. J.; McHale, G.; Newton, M. I.; Pyatt, F. B.; Doerr, S.H. Critical conditions for the wetting of soils. Appl. Phys. Lett. 2006, 89, 094101.

[62] Carlo Alberto Biffi, Paola Bassani, Jacopo Fiocchi, Donatella Giuranno, Rada Novakovic, Ausonio Tuissi, Enrica Ricci, Investigation of high temperature behavior of AlSi10Mg produced by selective laser melting, Materials Chemistry and Physics, Volume 259, 2021, 123975.